Editors' Suggestion | Featured in Physics

Juggling soliton: A new kind of wave-particle entity

Camila Sandivari,[1] Jacob Egge,[2] Belén Barraza,[1,*] Leonardo Gordillo,[3] and Nicolás Mujica[1]

[1]*Departamento de Física, Facultad de Ciencias Físicas y Matemáticas, Universidad de Chile, Santiago 8370449, Chile*

[2]*Universität Hamburg HX8M+JR, Hamburg, Germany*

[3]*Departamento de Física, Facultad de Ciencia, Universidad de Santiago de Chile, Estación Central 9170124, Chile*

(Received 10 June 2021; accepted 13 December 2022; published 10 February 2023)

We present an experimental study of a new kind of dual drop-wave entity existing on a localized structure in a water Faraday-wave system. A nonpropagating hydrodynamic soliton can juggle a single drop of ∼2–3.5 mm diameter for about 10^2–10^4 rebounds. By analyzing the drop trajectories, several regimes are observed: periodic bouncing, period doubling, period tripling, a sawtooth state, and chaotic/erratic trajectories. We present evidence that the most stable cases result from detuning of the drop self-oscillations and synchronization with the soliton's sloshing motion. This synchronization ensures stability and thus longer lifetimes. We analyzed the lifetime of the drop, concluding that the periodic behavior, which appears for the lowest-amplitude solitons, is the most stable state. Further analysis shows that lifetimes follow a Weibull distribution.

DOI: 10.1103/PhysRevFluids.8.024401

I. INTRODUCTION

The noncoalescence of drops in a bath of the same liquid has aroused a large amount of attention, in particular the stabilization of bouncing drops due to vertical vibrations of the liquid layer. Stable bouncing drops were first reported by Walker [1], in experiments using vibrated soap films. The fact that drops do not merge with the bath is quite counterintuitive, mainly because our daily experience, as well as some basic physics, tells us that a drop that is approaching a bath of the same liquid will tend to coalesce with it. Indeed, at short distances, van der Waals forces should tend to bring the two approaching surfaces together.

More recently, using a classical Faraday instability setup [2,3], but forcing below the pattern formation threshold, Couder *et al.* [4] demonstrated experimentally the crucial importance of a thin air layer that remains between the drop and the liquid surface. They show that the stability of the drop requires that the thin film of air, which provides the lift-off force and is trapped between the drop and the liquid bath surface, must be squeezed during the upward motion; during the downward motion, air must penetrate the film to allow for lift off; this idea was also presented by Walker [1]. Additionally, it has been shown that the bouncing drop lifetime depends on the driving acceleration and frequency [5]. The role of droplet deformations has also been analyzed to understand its bouncing dynamics [6–8].

Later, using liquids with lower viscosities, bouncing drops became amazingly interesting when the existence of a new kind of localized structure was experimentally demonstrated: the macroscopic

*Present Address: Advanced Mining Technology Center, Facultad de Ciencias Físicas y Matemáticas, Universidad de Chile, Avenida Tupper 2007, Santiago 8370451, Chile.

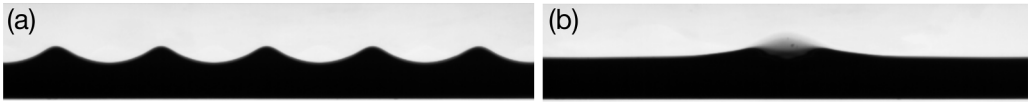

FIG. 1. Typical images of the two kinds of parametric instabilities that can be observed in the experimental setup: (a) Faraday waves and (b) NPHS. Both images were acquired using back-light illumination. For visualization purposes, a few drops of black ink are added to the liquid mixture (distilled water plus surfactant). The second instability has transverse movement, so a thinning of the liquid at the top of the soliton can be observed. As a reference, the depth of the layer of fluid is 2 cm. Images obtained from Gordillo [42].

wave-drop dual entity [9,10]. A series of experiments has shown macroscopic realizations of this wave-particle duality, reminiscent of quantum behaviors [11–18]. These results have motivated their theoretical understanding in terms of path-memory effects [19,20] and a hydrodynamic pilot-wave theory [21–23], inspired by the analogous quantum dynamics proposed by de Broglie. Thorough reviews of the walking-droplet system are those of Bush [24] and Bush and Oza [25].

Recently, there has been interest in the extension of the drop-wave dynamics above the Faraday instability, where the competition between the drop-generated waves and the wave field background becomes relevant. Sungar *et al.* [26] achieved droplet trapping in a liquid bath with a row of equally spaced immersed pillars: a hydrodynamic analog of the optical Talbot effect. Later, Tambasco *et al.* [27] presented an experimental study of the bouncing dynamics of droplets on the surface of the classical Faraday instability, also just above threshold. Several dynamical regimes are reported, including meandering, zigzag motion, erratic, trapping, and coalescence. In the erratic regime, a Brownian-like motion of the bouncing drop was characterized. Finally, Zhao *et al.* [28] studied the noncoalescence of drops in a high-surface-tension liquid-metal solution both below and above the Faraday instability. A single drop experiences several regimes as a function of its diameter and vibration acceleration, going from simple bouncing to period doubling below the Faraday threshold, and later to Faraday bouncing and chaotic bouncing as the acceleration is increased further. In this case, submillimeter droplets of liquid metal bounce at the antinodes of the Faraday pattern, the collisions with the bath occurring when the antinodes are wave troughs. They also studied the self-assembly of bouncing drops on top of the Faraday pattern.

Here we present an experimental study of a new kind of wave-particle entity. It is the *juggling soliton*: a localized sloshing wave that juggles a $\approx$2–3.5 millimeter-size drop. Both the drop and the surface wave are made of the same liquid, regular distilled water. Thus, our drops are much larger and both the drop and bath liquid are of much lower viscosity compared to most previous drop-vibrating surface studies. More precisely, we study bouncing drops on top of a nonpropagating hydrodynamic soliton (NPHS). This localized structure was first reported by Wu *et al.* [29] in a classical Faraday instability setup, when a quasi-one-dimensional rectangular basin (length $\gg$ width) that contains water is vertically vibrated within a range of frequencies and amplitudes. Figures 1(a) and 1(b) show, respectively, a pure longitudinal Faraday wave and a NPHS obtained in our experimental setup. The latter is obtained by perturbing the liquid-air interface with a sloshing movement using a one-inch-wide ruler.

Although these soliton waves keep the sloshing motion features of the first transverse surface mode (with a node in the longest axis of the cell), their motion is highly localized in the longitudinal direction instead of involving the whole surface [29]. For a single NPHS, its spatial envelope is steady, very stable, and does not propagate, in contrast with classical hydrodynamic solitons. When more NPHS are created, they can interact attractively or repulsively depending on their relative phase [30,31], form bounded states [30], and follow a coalescence process when several solitons are initially formed [32]. Remarkably, dissipative solitons can be found in several hydrodynamic systems: oscillons in a Faraday configuration [33] and solitary waves in vibrated Hele-Shaw cells [34] display spatial envelopes with similar spatiotemporal features.

NPHSs are modeled in terms of the parametric dissipative nonlinear Schrödinger equation (pdNLSE), derived by Miles [35], which captures the minimum requirements for parametrically

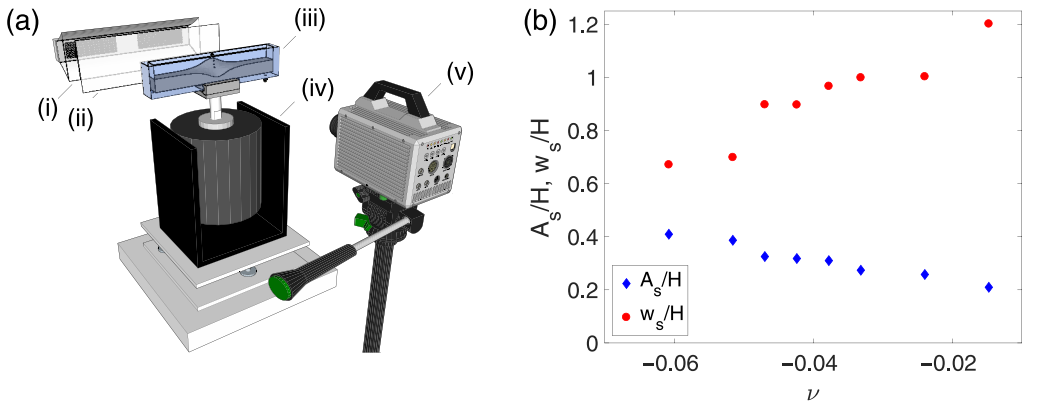

FIG. 2. (a) Illustration of the experimental setup, including the light-emitting diode arrangement (i), a white acrylic diffusive screen (ii), the acrylic basin (iii), the electromagnetic shaker (iv), and a high-speed camera (v). The driving acceleration is measured with a piezoelectric accelerometer. (b) NPHS characteristics as a function of reduced detuning $\nu = (f/2 - f_o)/f_o$, where $f_o = 5.43$ Hz is the resonant frequency of the first transverse mode. Its normalized amplitude A_s/H (width w_s/H) decreases (increases) as $\nu \to 0$.

sustained one-dimensional solitary structures. Hence, its scope goes far beyond hydrodynamics [36,37]. In this regard, recent studies have been focused on providing an exhaustive analysis of the pdNLSE using mathematical and numerical techniques. Experiments have also been used for this purpose [32,38,39]. On the contrary, some fundamental issues such as the validity of the approximations that yield the pdNLSE remain unaddressed, with rare systematic comparisons between predictions and measurements [40,41].

As for other localized structures, a simple argument that explains the NPHS existence is that its stability region corresponds to the parameter zone where both the flat interface and Faraday waves are possible solutions of the underlying dynamics; this corresponds to the negative detuning region of the first transverse mode, of frequency f_o. In this case, the subharmonic response frequency obeys $f/2 \lesssim f_o$, where f is the forcing frequency. Thus, following this simple argument, the localized NPHS arises as a connection between these two possible solutions, i.e., the first transverse mode and the flat, quiescent surface. The complete, more precise argument is that these localized structures are solutions of the pdNLS equation, that is, the amplitude equation that can be deduced from the Navier-Stokes equation plus the appropriate boundary conditions [35,42].

In our experiment, the localized surface wave, which acts as a juggler, keeps the drop bouncing centered at its maximum. The wave-drop motion is quite robust against lateral perturbations and thus the juggler spatially confines the drop. This configuration is a hydrodynamic analog of the optical tweezer using surface waves. Indeed, as in general for radiation pressure traps, the effective confinement depends on both the incident and scattered waves.

In this paper, we present the experimental setup and procedures in Sec. II, including some basic NPHS and drop characteristics. In Sec. III, we summarize the relevant dimensionless parameters and their values, also comparing them with previous studies; our low viscous large drops are indeed quite far from the usual parameter ranges. Then, in Sec. IV, we present our experimental results; we end this paper presenting our conclusions in Sec. V.

II. EXPERIMENTAL SETUP, PROCEDURES, AND GENERAL REMARKS

In Fig. 2(a), we present a schematic illustration of the experimental setup. The container is made out of acrylic and partially filled with a liquid mixture. The confining dimensions are width $L_y = 2.6$ cm, height $L_z = 5.5$ cm, and length $L_x = 20$ cm in the largest dimension. The liquid

mixture layer height is $H = 2\,\mathrm{cm}$. It is made from $200\,\mathrm{cm}^3$ of distilled water plus $2.7\,\mathrm{cm}^3$ of surfactant Kodak Photoflo, which is used to ensure good wall wetting during the soliton's sloshing motion [29]. On some occasions, a few drops of black ink are added to the liquid in order to obtain clear images of the soliton and the drop. Experiments are performed at room temperature, $T = 22$–$24\,^{\circ}\mathrm{C}$. The fluid's relevant parameters are dynamic viscosity $\mu \approx 0.93$ mPa s, mass density $\rho = 998\ \mathrm{kg/m}^3$, and surface tension $\sigma = 26.0 \pm 0.1$ mN/m. The latter was determined by the pending drop technique [43] using a Drop Shape Analyzer (Kruess GmbH model DSA-25E). The bouncing drops are composed of the same liquid mixture and they are made using a micropipette, which can be fixed at different volumes for ∼2–2.7 mm diameter drop's, or a plastic, disposable pipette for larger drops, ∼3.5 mm.

The forcing voltage waveform is created with a digital function generator (Agilent 33220A). A power amplifier (B&K model 2760) forces the electromechanical shaker (Dynamical Systems model VTS80). The container's vibration motion is measured using a piezoelectric accelerometer (B&K model 33640) firmly attached to the basin. The acceleration is sinusoidal, $a(t) = A\omega^2 \sin(\omega t)$, where A is the vibration amplitude and $\omega = 2\pi f$ is the driving angular frequency. The control parameter is the normalized acceleration $\Gamma = A\omega^2/g$, where g is the gravitational acceleration. The drop trajectories are obtained by standard digital image analysis techniques, using sequences recorded with a high-speed camera, typically at 200 or 400 fps (depending on the particular experiment, we use one of these high-speed cameras: Ditect HAS-EF or Phantom v641).

We performed experiments for forcing frequencies in the range $f = 10.2$–10.8 Hz. The first transverse mode frequency was determined experimentally, $f_o^{\mathrm{exp}} = 5.39 \pm 0.07\,\mathrm{Hz}$, by means of measuring the surface response under a slowly varying frequency forcing, at low amplitude, using a height resistive sensor composed of two parallel wires immersed in the liquid layer. Many longitudinal modes as well as the first transverse one can be identified. The theoretical value is given by the surface gravito-capillary wave dispersion relation using the appropriate boundary conditions, $f_o^{\mathrm{theo}} = 5.43 \pm 0.06\,\mathrm{Hz}$, with the error originating from the precision with which the experimental geometrical and physical parameters are known. As expected, both values agree within experimental errors. Details of the experimental method and theoretical analysis can be found in [42]. We define the reduced detuning parameter $\nu = (f_s - f_o)/f_o$, where $f_s = f/2$ is the soliton frequency, and we choose to use the theoretical value $f_o \equiv f_o^{\mathrm{theo}}$.

The soliton alone has a well-established stability region [29]. A negative detuning is a necessary condition, which is the region for which the Faraday instability is subcritical. The NPHS shape depends on the detuning parameter, as shown in Fig. 2(b). Its amplitude A_s and width w_s decrease and increase, respectively, as the subharmonic response f_s approaches the first transverse mode frequency f_o. For the data shown in Fig. 2(b), both quantities are obtained by fitting the soliton shape with the function $A_s \mathrm{sech}[(x - x_o)/w_s]$, where x_o corresponds to the soliton's central position [31]. We notice that as expected, $A_s w_s$ is constant as a function of ν. Indeed, we obtain $A_s w_s = 110 \pm 6\,\mathrm{mm}^2$.

Once a stable NPHS is formed in the vibrated basin, a drop made from the same fluid is placed over its surface. If the size of the drop and the time of release are appropriate, the drop will bounce periodically with period $T = 2/f$, equal to the soliton's period, which is twice the forcing one. The periodic action of the soliton wave, relaunching the drop at every cycle, recalls the action of a juggler. Stable *juggling soliton* structures have been obtained for drop diameters $D = 1.8$–3.8 mm and lifetimes that last from a few minutes up to about 90 min, which implies about 10^3–10^4 stable rebounds.

Drops of about 2.5 mm diameter are generated using the micropipette with a volume fixed to 10 µl. Larger drops are made using a plastic, disposable pipette. In Sec. IV, we present a phase diagram survey of drop stability with the smaller drops. We analyzed 459 realizations at different driving frequency f and forcing acceleration Γ. In Fig. 3, we present the drop-diameter histogram for all these realizations. For each drop, D was obtained from calibrated image analysis of all

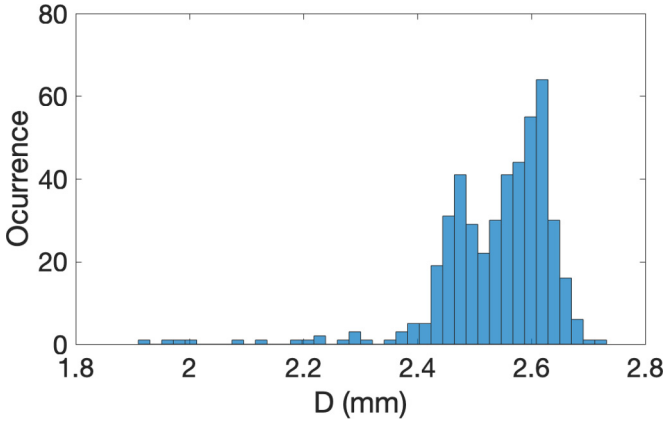

FIG. 3. Drop-diameter histogram. Drops are generated using a micropipette with a volume fixed to 10 μl. Most drops (84%) are concentrated in the range $D = 2.54 \pm 0.10$ mm.

those stable juggling soliton realizations that we got in the phase diagram survey. Most drops are indeed concentrated around 2.5 mm, the average being $\langle D \rangle = 2.54$ mm and its standard deviation $\sigma(D) = 0.10$ mm.

III. DIMENSIONLESS NUMBERS

The bouncing drops of the juggling soliton are larger and less viscous than those previously studied. In order to independently compare to previous studies, we summarize the relevant physical variables and the dimensionless numbers of the drop impact on a NPHS for the case where the drop and the liquid surface are both composed of distilled water with a small amount of surfactant Photoflo. The physical parameters are the drop's diameter D, the drop's effective acceleration g_{eff}, impact velocity v_o, and the liquid dynamic viscosity μ, density ρ, and surface tension σ. From these six parameters, we can define three independent dimensionless numbers, plus a fourth dimensionless parameter given by the forcing angular frequency $\omega = 2\pi f$. Thus, we have the following:

(i) The Ohnesorge number $\text{Oh} = \mu\sqrt{1/(\rho\sigma D)}$, which compares viscous and capillary times. In our system, Oh = 0.003–0.004. Thus, capillary waves are relevant both on the surface of the soliton and the drop.

(ii) The Bond number, $\text{Bo} = \rho g_{\text{eff}} D^2/(4\sigma)$, with g_{eff} the drop's effective acceleration. This number compares gravitational and capillary energies. During take off, we estimate $g_{\text{eff}} = g_{\text{rel}} \approx$ 3–4 m/s^2 as the relative acceleration between the NPHS wave acceleration and the gravitational acceleration. The upper limit considers the meniscus correction. For drop sizes $D = 2$–3.5 mm, Bo = 0.1–0.5. During free flight, $g_{\text{eff}} = g$, the gravitational acceleration. In this case, Bo = 0.4–1.2.

(iii) The Weber number, $\text{We} = \rho D v_o^2/(2\sigma)$, which compares the incoming drop kinetic and surface energies. For $D = 2.7$ mm, we measured $v_o \approx 0.1$ m/s. Considering this a typical "catching" velocity scale, we get We ≈ 0.4–0.7 for drops in the range $D = 2$–3.5 mm.

(iv) The vibration number $\Omega = \omega/\omega_D$, where $\omega_D = \sqrt{\sigma/\rho R^3}$ is the characteristic drop-oscillation frequency and $R = D/2$ is the drop radius. In our experiments, Ω = 0.4–1.

In Table I, we summarize the values of the dimensionless numbers for the experiments reported in this article, as well as those of the previous studies of bouncing drops on Faraday waves. We also include the values reported by Moláček and Bush [6], as a representative example of the bouncing drop below the Faraday instability.

Our Oh parameter is considerably lower than all those reported in previous bouncing drop experiments, where the liquid viscosity is much larger. Terwagne *et al.* [7] summarize the studies up to date in a Oh_d versus Oh_b diagram, where Oh is defined independently for the drop and the

TABLE I. Dimensionless numbers for the present work and previous experiments of bouncing drops on Faraday waves [26–28]. In the case of Zhao *et al.* [28], we report the Oh values of the NaOh solution, which is much more viscous than the GaIn alloy; it is thus expected to dominate the interface wave dynamics. Also, Bo and Ω are computed with the density difference $\Delta\rho = \rho_{\mathrm{GaIn}} - \rho_{\mathrm{NaOh}}$. We also include the values reported for bouncing drops below the Faraday threshold by Moláček and Bush [6], as a representative example of those systems. The asterisk * stands for estimated values, as for these experiments they use the same silicone oils and drop sizes as in [6].

Dimensionless number	Oh	Bo	We	Ω
Present study	0.003–0.004	0.1–1.2	0.4–0.7	0.4–1
Sungar *et al.* [26]	0.2	0.07	0.01–1*	0.6–0.9
Tambasco *et al.* [27]	0.1–0.8	0.005–0.1	0.01–1*	0.1–1.2
Zhao *et al.* [28]	1.5–3.0	0.002–0.04		0.02–0.8
Moláček and Bush [6]	0.1–0.8	0.005–0.2	0.01–1	0–1.4

bath. All studies obey $\mathrm{Oh}_d > 0.01/\sqrt{\mathrm{Oh}_b}$. Our experiment, for which $\mathrm{Oh}_d = \mathrm{Oh}_b \sim 0.001$, remains very far from this boundary; thus, the induced drop deformations and surface waves do not decay quickly due to viscosity. However, the waves created on top of the NPHS do decay before the drop's next take off. Also, these waves are emitted far away from the drop-impact position. In addition, we observe that both the drop and the NPHS interface deform strongly during their contact time and for the drop's free-flight period as well.

Because of our drop sizes, Bo is much larger in the present study than the values of the experiments reported by Moláček and Bush [6], for the bouncing drop below the Faraday instability, and also larger than the previous studies above this instability [26–28]. Our minimum Bo is in the upper range of Moláček and Bush [6] and Tambasco *et al.* [27], and our maximum Bo is ∼10 times larger than this minimum value. Finally, our We is rather in the high value range of previous studies. These facts are a consequence of our larger drop sizes and also the larger energies involved; our drops are launched by the NPHS to heights between 5 and 20 mm above the quiescent liquid-surface level, which also implies much larger absolute velocities at impact. However, the relative velocity between the drop and the NPHS is lower, as the surface wave rather gently catches the drop during its descending motion.

IV. EXPERIMENTAL RESULTS

A. Drop dynamics and phase diagram

In this section, we focus on experiments for the drop diameter $D \approx 2.5$ mm, and some results are also given for larger drops in the following sections, with $D = 3$–3.5 mm. Once a drop is placed on top of the sloshing soliton, its trajectory is studied analyzing front, side, and top views of the basin that holds the NPHS, although for most of the results, we focus on the front-view characterization. Representative images are shown in Fig. 4 and some videos are available in the Supplemental Material [44]. The front view reveals that during free flight, the drop's trajectory is parabolic, which can be fitted to obtain the effective vertical acceleration g_{eff}; this is presented and discussed below. As stated in the previous section, the Oh number is very low, which is reflected in the drop oscillations and the surface waves induced on top of the NPHS. The former occurs during the complete soliton period, but is particularly stronger during the drop's free flight. This analysis will also be presented in detail. This fact, combined with the relatively high Bo number, implies that these oscillations last longer in time and are larger in amplitude. This is shown in Figs. 4(b) and 4(c), where the deep drop penetration into the surface, its strong deformations during free flight, and the surface waves that are emitted can be observed (the latter are clearly observed in the video presented in the Supplemental Material [44]).

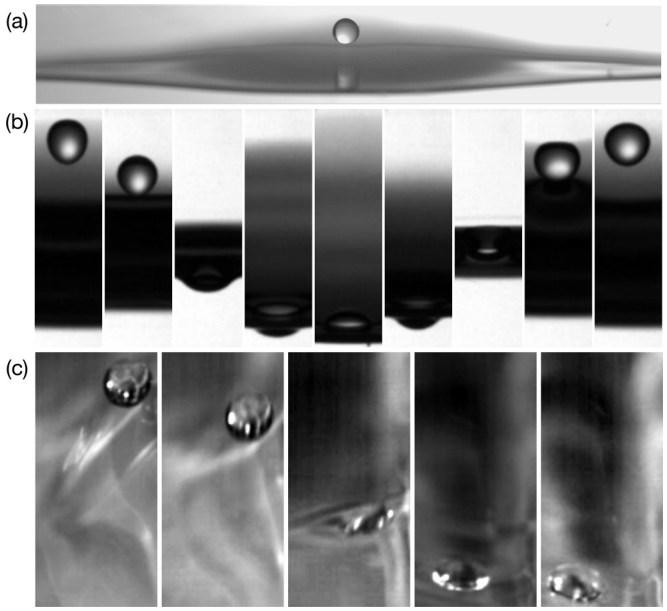

FIG. 4. (a) Front-view image of a ∼3.5 mm diameter drop that bounces over a NPHS, with forcing frequency $f = 10.4$ Hz and acceleration $\Gamma = 0.085$ (the same for all panels). (b) Sequence of images of a 2.7-mm-diameter drop bouncing over a NPHS, showing an almost complete cycle of the drop motion (total time 0.2 s, soliton period $1/5.2 \approx 0.192$ s; time lapse between frames is 25 ms). The drop strongly deforms during the rebound, as well as the soliton's surface. The drop oscillates in its fundamental mode all the time, although more strongly during the free-flight period. (c) Side view of the same drop shown in (b). Here, half a period is shown, with the same time lapse between frames. Surface waves generated at the collision are visible.

The drop's transverse motion is more complex. An example of a (y, z) trajectory, obtained by a lateral view, is shown in Fig. 5(a). The blue dots connected by lines show the drop's center of mass; the solid red line is a guide to the eye of the parabolic motion during free flight; and the black arrows indicate the drop motion direction. The lateral coordinate origin ($y = 0$) is arbitrary, but we notice that during the drop's ascending motion and particularly at take off, it is almost in contact with the wall. The vertical origin ($z = 0$) is fixed at the liquid-surface quiescent level (horizontal black dashed line). We observe that the drop is released from the surface of the soliton almost at the peak of the wave's trajectory, and that the free flight lasts about $1/3$ of the complete soliton period. The drop is literally catched by the NPHS when they are both descending, at a distance about $1.1D$ from the lateral wall. This occurs very close to $z = 0$, so the soliton interface at the catching time is almost flat. This can also be observed in the third image of Fig. 4(b), which shows the drop shortly after it has been catched by the NPHS. The lateral and vertical drop center of mass position versus time is presented in Figs. 5(b) and 5(c). These are nonlinear periodic functions of time. The drop transverse motion is fast during the descending and ascending wave periods of time, and slows down at the reversals. As the drop is on its way to reach the soliton maximum height, the wave throws the drop upward. The drop detachment is due to the wave's slowing down. Finally, from these image sequences and trajectory analysis, we determined that the relative impact velocity is $v_o \approx 0.1$ m/s and that the relative acceleration at take off is $g_{\text{rel}} \approx 3$–4 m/s^2, with the same direction as the gravitational acceleration. These numbers were used for the estimation of both We and Bo.

Examples of the drop's center-of-mass height-time trajectories, obtained from front-view images, are shown in Fig. 6. Only during free flight can its position be precisely detected, leading to gaps between data points. Three regimes are identified, by simply observing the height maxima, and examples are shown in this figure: periodic bouncing at frequency f_s [Fig. 6(a)], period doubling,

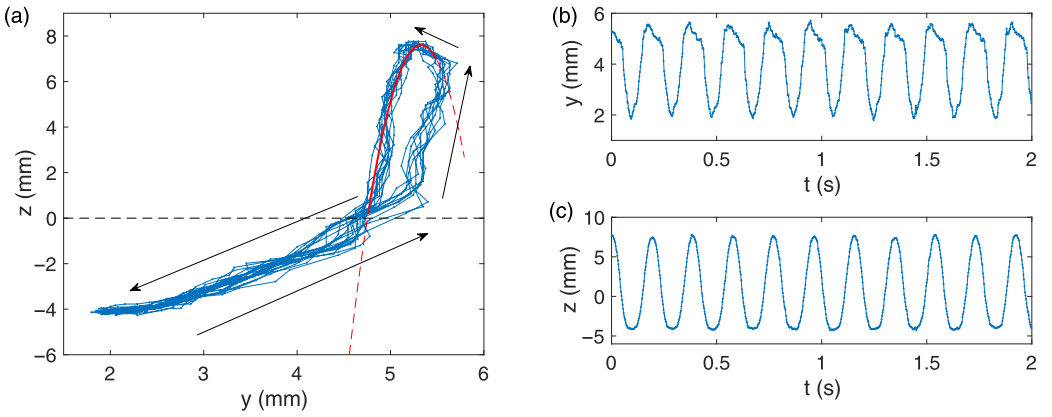

FIG. 5. (a) Trajectory of a 2.7-mm-diameter drop in the (y, z) plane obtained by a lateral view, with forcing frequency $f = 10.4$ Hz and acceleration $\Gamma = 0.085$ [same drop shown in Fig. 4(c)]. Arrows indicate the drop motion direction. The solid red line shows a parabola as a guide to the eye for the drop's free-flight period and the horizontal black dashed line shows the liquid-surface quiescent position ($z = 0$). The transverse and vertical positions vs time are presented in (b) and (c).

bouncing at frequency $2f_s$ [Fig. 6(b)], and an apparent chaotic/erratic motion [Fig. 6(c)], with irregular heights. These dynamical regimes are similar to those found by Zhao *et al.* [28] in experiments of bouncing drops on top of a Faraday wave in a liquid gallium-indium alloy below a NaOH solution. In Fig. 6(d), we present the height fluctuations versus the time difference between successive maximum heights of the free-fall drop. The regular, period doubling, and erratic cases are clearly distinguishable. The first case concentrates around (1,0), and the second shows two distinctive maxima, with the lower (higher) one that has a shorter (larger) period, but still remains

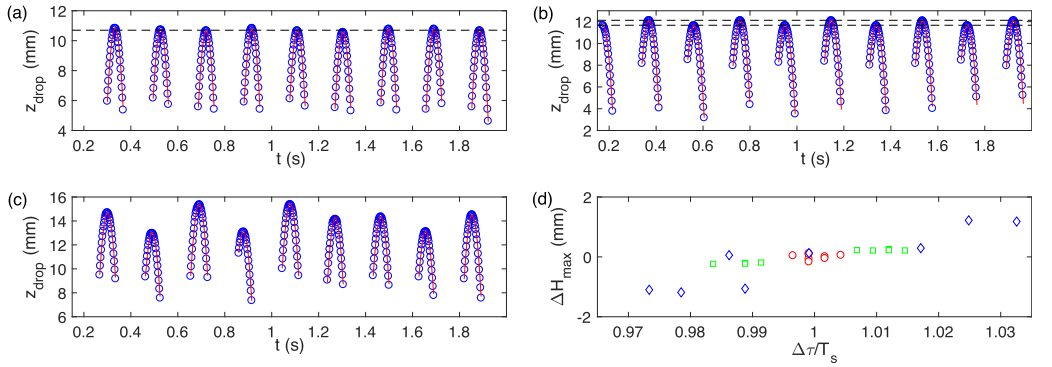

FIG. 6. Examples of possible drop's height-time trajectories, obtained from front-view images. (a) Regular periodic rebounds, $f = 10.2$ Hz, $\Gamma = 0.1122$, and $D = 2.43$ mm. (b) Double period rebounds, $f = 10.3$ Hz, $\Gamma = 0.097$, and $D = 2.52$ mm. (c) Chaotic/erratic rebounds, $f = 10.3$ Hz, $\Gamma = 0.1122$ and $D = 2.49$ mm. The solid (red) lines show the parabolic fits. The averages for all the adjusted effective accelerations are (a) $g_{\text{eff}} = 9.1 \pm 0.1\,\text{ms}^{-2}$, (b) $g_{\text{eff}} = 9.1 \pm 0.2\,\text{ms}^{-2}$, and (c) $g_{\text{eff}} = 9.4 \pm 0.2\,\text{ms}^{-2}$. The horizontal dashed lines show (a) the regular height average and (b) two distinctive heights for the doubling period case. (d) Height fluctuations $\Delta H_{\text{max}} = H^i_{\text{max}} - \langle H_{\text{max}} \rangle$ vs the normalized time difference between successive maxima, with $\Delta\tau = t^i_{\text{max}} - t^{i-1}_{\text{max}}$ the time difference between successive maxima, and $T_s = f_s^{-1}$ the soliton period, for regular periodic rebounds (○), double period rebounds (□), and erratic bouncing (◇).

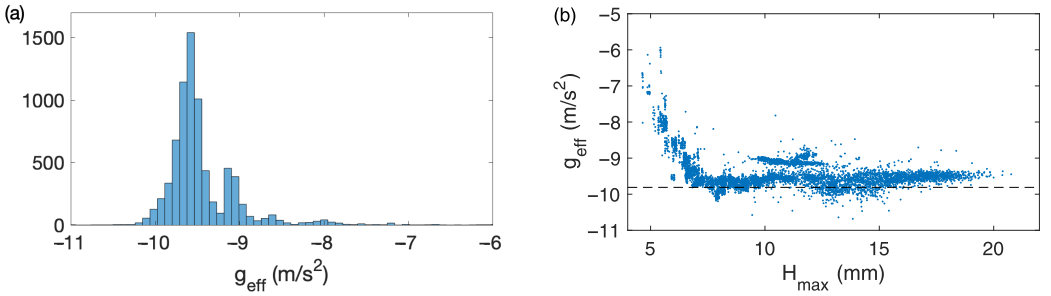

FIG. 7. (a) Histogram of adjusted effective gravitational acceleration g_{eff} for all measured drop parabolic trajectories. Most cases are indeed close to the gravitational acceleration $g = -9.81\,\text{ms}^{-2}$. (b) g_{eff} vs maximum drop height H_{max}. The horizontal dashed line corresponds to the gravitational acceleration g. Lower trajectories have a smaller effective acceleration, probably due to a stronger viscous drag by the air layer between the drop and the NPHS surface.

close to (1,0). The erratic case expands the values further away from (1,0), randomly filling a somewhat linear behavior between the quantities.

The effective acceleration g_{eff} varies from $-11.0\,\text{ms}^{-2}$ to $-6\,\text{ms}^{-2}$ among realizations, with most cases close to the gravitational acceleration $g = -9.81\,\text{ms}^{-2}$. Figure 7 displays the histogram of the measured g_{eff} and its dependence on the maximum drop height H_{max}. Drops with lower maximum heights are subject to smaller effective accelerations and remain very close to the soliton wave throughout its motion. In fact, the soliton amplitude varies from a few mm to ∼1 cm, exactly within the range where g_{eff} changes from an approximate constant value (with dispersion) to a quantity that increases for decreasing H_{max}. For such small-amplitude NPHS, the drop can be detected by image analysis only because the very thin water layer at the wall can be seen through. We have checked indeed that it remains in contact with the wave surface most of the time. Thus, we conclude that during the apparent free-flight period, the drop is experiencing some additional aerodynamic force originated from its closeness to the NPHS surface, probably due to air entrainment. This would explain its lower effective acceleration.

The trajectories shown in Fig. 6 correspond to three realizations of a large survey in the frequency and acceleration phase space. We stress that at a given frequency and acceleration (f, Γ), in some occasions more than one of the possible regimes can occur; they coexist in the parameter space. Thus, for each frequency in the range 10.2–10.8 Hz, with a step of 0.1 Hz, we did acceleration ramps between $\Gamma \approx 0.1$ and $\Gamma \approx 0.2$, with steps $\Delta\Gamma \approx 0.01$. For each pair (f, Γ), about 20 realizations were done and, in each case, a new drop was created and placed above the NPHS. When it was found to bounce in a stable position, it was recorded at 400 fps, for 2 s, which is the equivalent of about 8–10 rebounds, as the examples show in Fig. 6. Stable bouncing drops were found in the range 10.2–10.7 Hz ($\Delta f = 0.1$ Hz), with the detuning parameters indicated in Table II.

A summary of this survey is shown in Fig. 8, where the phase diagram (ν, Γ) is presented. At a fixed forcing frequency f, but with the subharmonic response f_s below the first transverse mode f_o, we slightly increase the driving vibration amplitude A. At each fixed A, we manually perturb the flat, quiescent surface using a paddle. The perturbation is done locally and with a transverse sloshing motion that emulates the NPHS motion. When done correctly, the soliton appears and

TABLE II. Detuning parameter for each forcing frequency.

Frequency f (Hz)	10.2	10.3	10.4	10.5	10.6	10.7
Detuning parameter ν	-0.061 ± 0.011	-0.052 ± 0.011	-0.042 ± 0.011	-0.033 ± 0.011	-0.024 ± 0.011	-0.015 ± 0.011

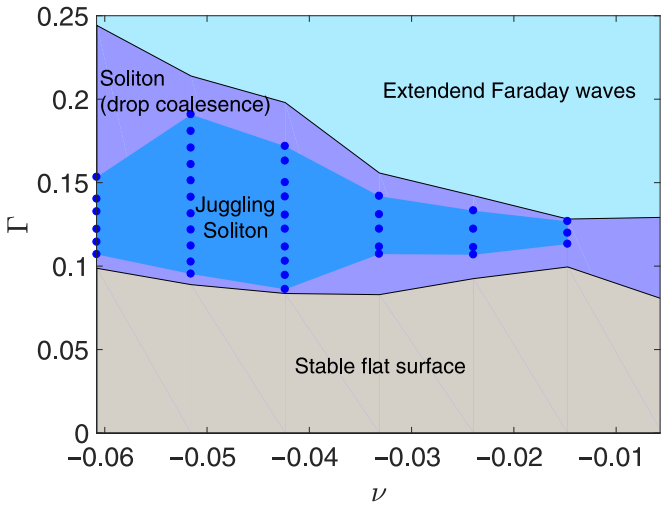

FIG. 8. Experimental phase diagram (ν, Γ). The single drop juggling soliton is stable in a subregion of the stability region of the NPHS alone. Most of the drops are in the range $D = 2.44$–2.64 mm. The data points show the (ν, Γ) values that have been studied where single drop stable juggling solitons are found, with the conditions explained in the text (stable realizations recorded for 2 s, equivalent to 8–10 rebounds).

becomes stable. The system can sustain a single NPHS in the region shown in Fig. 8. Its lower and upper Γ limits are close to the theoretical expectation: an almost flat, constant lower-Γ limit and a paraboliclike shape for the upper-Γ limit, which is the negative part of the first transverse mode's Arnold tongue [31]. The single drop juggling soliton is stable in a subregion of the NPHS existence region, shown in blue with data points in Fig. 8. Recall that at least 20 stable juggling solitons were done for each (ν, Γ), and that for each case, more than one regime can be observed. This multistability is probably due to different drop release initial conditions and small variations in size.

In order to better characterize the different dynamical regimes, for each realization we compute the series of drop maximum heights H_n. In Fig. 9, we present the return maps, H_n vs H_{n+1}, for all the realizations obtained in the previously stated phase-space region (ν, Γ). Periodic trajectories correspond to those data point sets that fall in the identity line $H_n = H_{n+1}$, period doubling to those symmetrically opposed to this line, and the other, apparently chaotic trajectories are all those data points that do not fall in these categories. More quantitatively, for each set H_n, we compute its average $\langle H_n \rangle$ and standard deviation $\sigma(H_n)$. If

$$\frac{\sigma(H_n)}{\langle H_n \rangle} < 0.02, \tag{1}$$

then the trajectory is classified as periodic. If this is not satisfied, then the subsets H_{2n} and H_{2n+1} are compared. If

$$|\langle H_{2n} \rangle - \langle H_{2n+1} \rangle| > 3\sqrt{\sigma(H_{2n})^2 + \sigma(H_{2n+1})^2}, \tag{2}$$

then H_n is considered to be alternating between two distinct heights. Everything else is considered to be other/erratic behavior. The three regimes are classified in color code in Fig. 9, with red for periodic, green for doubling period, and blue for the other/erratic trajectories. The most interesting cases are observed for frequencies 10.2 Hz, 10.3 Hz, and 10.4 Hz, for which the three possible dynamical regimes compete. In Fig. 10, we show histograms of the height deviations, with respect to their means, for these cases. The three possible dynamical regimes are plotted separately, showing their relative occurrence. The 1-period case is indeed concentrated at the origin, the 2-period case

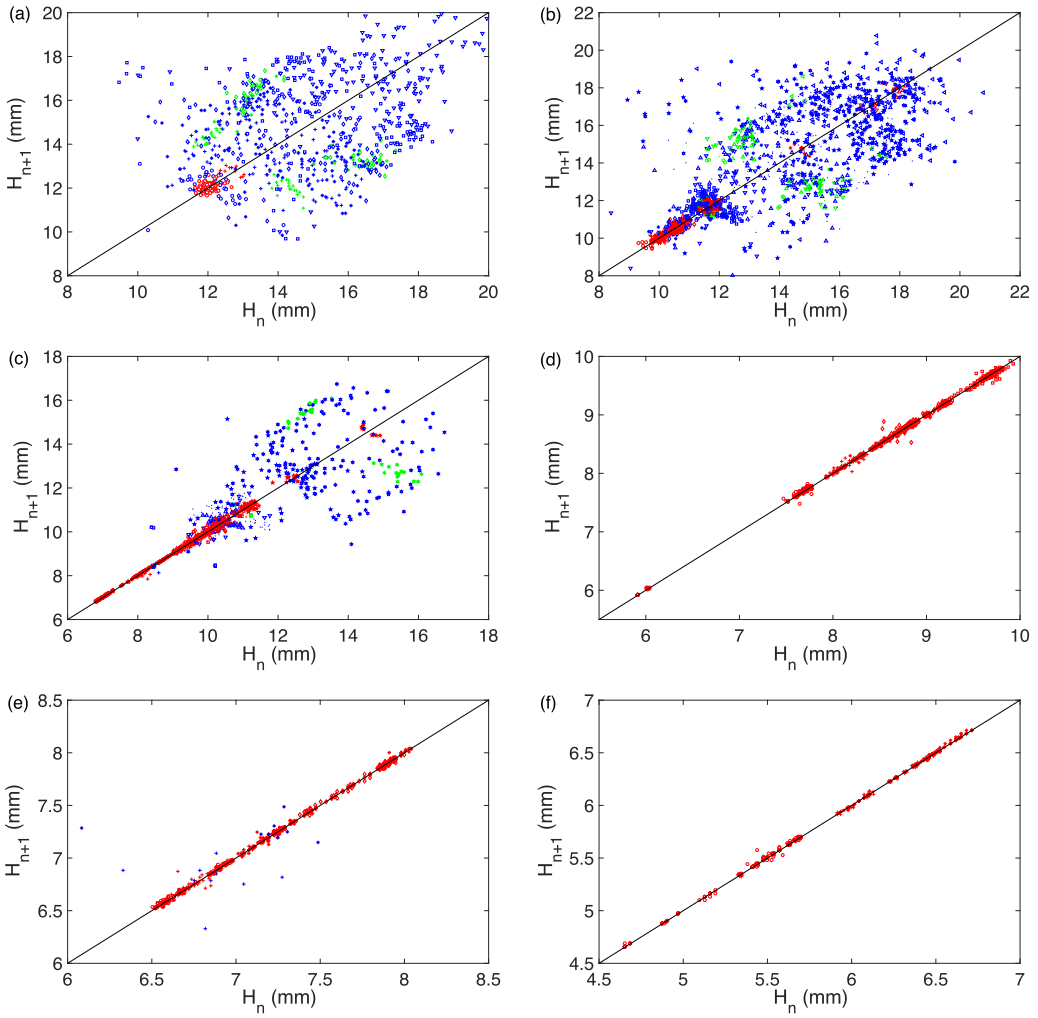

FIG. 9. Examples of possible drop dynamics, visualized through return maps (H_n, H_{n+1}), for all Γ and (a) $f = 10.2\,\mathrm{Hz}$, (b) $f = 10.3\,\mathrm{Hz}$, (c) $f = 10.4\,\mathrm{Hz}$, (d) $f = 10.5\,\mathrm{Hz}$, (e) $f = 10.6\,\mathrm{Hz}$, and (f) $f = 10.7\,\mathrm{Hz}$. The periodic, doubling period, and erratic cases are shown in red, green, and blue, respectively.

distributes symmetrically around the origin, and the chaotic/other cases are more widely spread. Figure 11 shows the relative occurrence of each state at different Γ for these same frequencies. The simple periodic state is more likely to occur for $f = 10.2\,\mathrm{Hz}$ and $f = 10.3\,\mathrm{Hz}$ in limited ranges of Γ, and also for $f \geqslant 10.4\,\mathrm{Hz}$ for almost all Γ in the stability region of the juggling soliton at these frequencies [see, also, Figs. 9(d)–9(f)].

B. Drop oscillations, self-detuning, and drop-wave synchronization

The role of drop oscillations has been studied in order to get a better insight into the bouncing droplet dynamics. The drop has been modeled as two masses linked by a linear spring with dissipation [6–8], which is vibrated by a liquid interface that in turn is modeled as a more "rigid" surface ($\mathrm{Oh}_b \gg \mathrm{Oh}_d$). A mass asymmetry has also been considered to account for the asymmetric deformations of the larger drops [8]. A logarithmic spring model has also been considered for $\mathrm{We} > 1$, where the contact time and effective restitution coefficient have been measured to depend

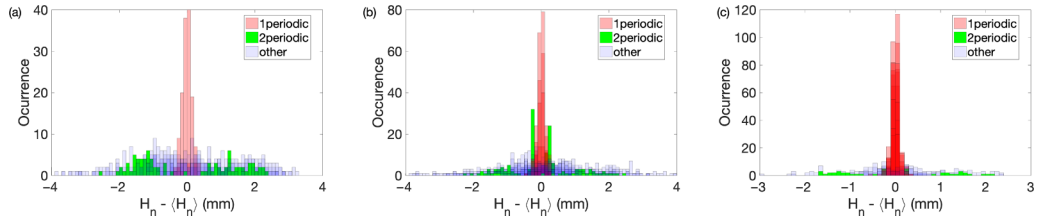

FIG. 10. Histograms of height deviations $H_n - \langle H_n \rangle$, for (a) $f = 10.2\,\mathrm{Hz}$, (b) $f = 10.3\,\mathrm{Hz}$, and (c) $f = 10.4\,\mathrm{Hz}$. The periodic, doubling period, and erratic cases are shown in red, green, and blue, respectively.

logarithmically on We [6]. These studies show that the different bouncing drop dynamical regimes can be understood in terms of their surface-mode resonance, or antiresonance in some cases, and how they couple with the vibrated liquid surface.

As briefly mentioned earlier, our bouncing drops also oscillate during their free flight above the NPHS, with an amplitude of about 10% of their radius. So, some natural questions arise: At which frequency do they oscillate? How does this affect the stability of the juggling soliton as a whole, considering that the drop is oscillating at the collision, and catch-up by the NPHS?

To answer these questions, we performed experiments at specific forcing frequencies and different drop sizes. During its free flight, the drop diameter is measured through image analysis, by detecting its center of mass and the drop's horizontal width at this vertical position. This is obtained with a subpixel resolution by fitting an appropriate hyperbolic tangent function to the image intensity profile at the center-of-mass vertical position.

In Fig. 12, we present a first example of drop-oscillation analysis, for $f = 10.4\,\mathrm{Hz}$ and $\Gamma = 0.112$, and drop average diameter $D \approx 2.7\,\mathrm{mm}$. The NPHS subharmonic nature is evident when one compares the soliton amplitude A_s time evolution with the cell's base oscillation. When A_s is compared to the drop's center-of-mass motion, we deduce that the drop is released by the NPHS when it is about to arrive at its maximum, and is catched-up later when the soliton is almost flat. During its free flight, the drop oscillates at what seems to be its first resonant mode, with alternating elongations and contractions in the vertical and horizontal directions. Figure 12(c) presents the drop-diameter oscillations for these two free-flight events. The adjustment of the complete data set, corresponding to four rebounds, to a single sinusoidal function works quite well, with an average drop diameter $D = 2.670 \pm 0.004\,\mathrm{mm}$ and oscillation frequency $f_d = 52.04 \pm 0.07\,\mathrm{Hz}$, which is very close to 10 times the NPHS frequency $f_s = 5.2\,\mathrm{Hz}$. The same analysis was done for 20 consecutive rebounds, fitting again the same sinusoidal function, for which we obtained $f_d = 52.002 \pm 0.002\,\mathrm{Hz}$. Thus, the drop synchronizes to the wave sloshing motion, $f_d = 10 f_s$. We speculate that this insures stability and, probably, a longer lifetime.

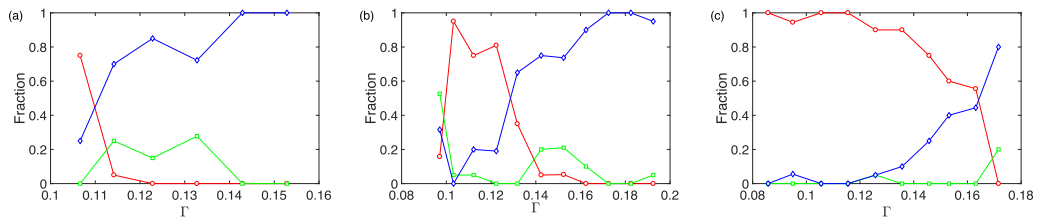

FIG. 11. Occupation fraction of each dynamical regime as function of Γ, for (a) $f = 10.2\,\mathrm{Hz}$, (b) $f = 10.3\,\mathrm{Hz}$, and (c) $f = 10.4\,\mathrm{Hz}$. The symbols correspond to regular periodic (○), periodic doubling (□), and erratic (◇).

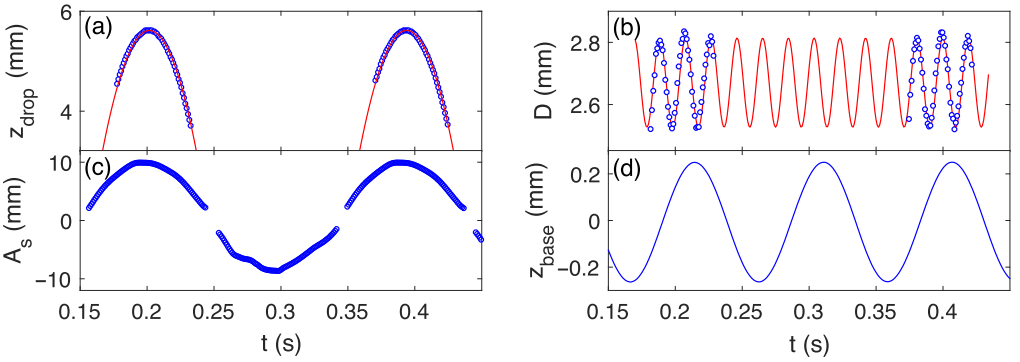

FIG. 12. Drop oscillations during two rebounds at $f = 10.4$ Hz and $\Gamma = 0.112$. (a) Drop center of mass vs time; the parabolic flights are fitted with $g_{\text{eff}} = 9.82 \pm 0.10\,\text{ms}^{-2}$ and $g_{\text{eff}} = 9.81 \pm 0.08\,\text{ms}^{-2}$, respectively. (b) Drop diameter D vs time. The complete data set is fitted with a single sinusoidal function, $D(t) = D + a_d \sin(2\pi f_d t + \phi)$, with $D = 2.670 \pm 0.004$ mm, $a_d = 0.143 \pm 0.007$ mm, and $f_d = 52.04 \pm 0.07$ Hz. (c) Soliton amplitude A_s as a function of time. (d) The cell's base oscillation.

The drop resonant frequencies are given by [45]

$$\omega_o^2 = \frac{\sigma\,\ell(\ell-1)(\ell+2)}{\rho R^3}, \tag{3}$$

and the fundamental frequency is obtained for $\ell = 2$. For the drop of Fig. 12, with $D = 2.67$ mm and $\sigma = 26\,\text{mN m}^{-1}$, $f_o = \omega_o/(2\pi) = 47.1$ Hz. Thus, the drop not only synchronizes with the NPHS, but, in order to do so, its oscillation is detuned with respect to its fundamental resonant mode, in about 10% in this case.

To confirm our findings, we did some experiments with larger drops, at the same experimental conditions. Using a plastic, disposable pipette, we can generate larger drops, of about 3.5 mm diameter, which can also bounce over the NPHS, forming a juggling soliton. Three realizations with larger drops were analyzed. A typical result is shown in Fig. 13, for which we analyzed nine rebounds. Here, the drop is in the period doubling regime, showing slightly different maximum heights and diameter oscillations every two periods. The ∼0.05 mm larger oscillations of the drop have maximum heights (not shown) that are ∼1 mm greater than the smaller ones. We fitted sinusoidal functions separately for each subset of data and, in both cases, we obtain $f_d = 31.20 \pm 0.02$ Hz. Thus, the oscillation frequency is $f_d = 6 f_s$. The natural frequency for this drop size is $f_o = 30.7$ Hz, so the drop is detuned about 1.8%. For the other two large drop cases that we analyzed, one was also

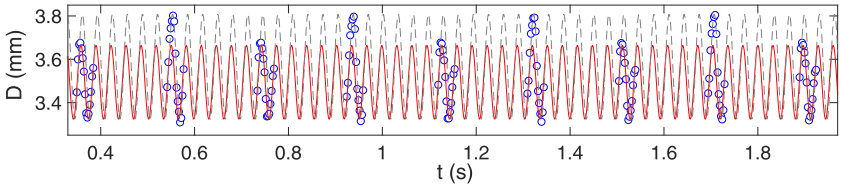

FIG. 13. Example of drop oscillations for a larger drop, $f = 10.4$ Hz and $\Gamma = 0.115$; in this case, for nine rebounds in the period doubling regime. Each subset is fitted with a single sinusoidal function, $D(t) = D + a_d \sin(2\pi f_d t + \phi)$, with $D = 3.56 \pm 0.01$ mm, $a_d = 0.23 \pm 0.01$ mm for the larger oscillations of the drop (dashed line) and $D = 3.50 \pm 0.01$ mm, $a_d = 0.17 \pm 0.09$ mm for the smaller oscillations of the drop (solid line). In both cases, the adjusted drop frequency is $f_d = 31.20 \pm 0.02$ Hz. The mean diameters are different by ≈1.7%. We believe this is due to nonlinear deformations of the drop (very elongated states), which are probably different between two consecutive rebounds in the period doubling state.

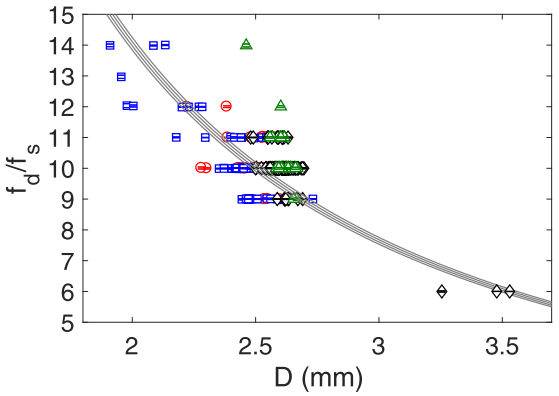

FIG. 14. Normalized oscillation frequency f_d/f_s vs drop diameter D, for $f = 10.2$ Hz (○), 10.3 Hz (□), 10.4 Hz (◇), and 10.5 Hz (△). The solid lines correspond to the theoretical normalized fundamental frequency f_o/f_s, given by Eq. (3). The measured possible drop's oscillation frequencies are $f_d = 9f_s$, $10f_s$, $11f_s$, $12f_s$, $13f_s$, and $14f_s$ for the smaller drops, and $f_d = 6f_s$ for the larger ones. Synchronization and detuning are evident from the levels and frequency variations with respect to f_o/f_s. For each large drop in the period doubling regime, their diameters and oscillation frequencies were averaged.

in the period doubling regime, with 19 analyzed rebounds in total, and the other one in an erratic state, with 20 analyzed rebounds. For the latter, we fitted the complete set of data with a single sinusoidal function. In these two cases, we also measured $f_d = 6f_s$.

Analyzing all the data of the phase diagram survey of the previous section, that is, for $D \approx 2.5$ mm, we found that other cases are also possible. Between 10.2 and 10.5 Hz, and for all the Γ explored, we found that all these cases occur: $f_d = 9f_s$, $10f_s$, $11f_s$, $12f_s$, $13f_s$, and $14f_s$. The different synchronizations and detunings are due to variations in drop diameter, which actually vary between ≈1.9 mm and ≈2.7 mm, but with most cases around 2.5 mm. The summary of the collected data, including the larger drop cases, is presented in Fig. 14. The total number of analyzed drops is 462 (459 small drops generated with the micropipette plus the 3 larger ones). The drop's frequency synchronization and detuning is clearly demonstrated. The solid lines correspond to the theoretical predictions f_o/f_s, with f_o given by Eq. (3), using the measured surface tension, $\sigma = 26\,\mathrm{mN\,m^{-1}}$. Figure 14 also shows that drops of the same size can bounce by undergoing a different number of oscillations within a single forcing cycle. Thus, the dynamic system does require an additional number for a complete description compared to other bouncing drop systems (e.g., [24]), i.e., the number of drop-oscillation cycles per forcing or wave/liquid bath period. This feature enriches the landscape of resonances and antiresonances documented by Hubert *et al.* [8] by adding contiguous higher-order harmonics drop modes because of the enlarged size of the drop. Further meticulous experimental analysis is required to better understand the allowed bands of drop sizes that the soliton wave can juggle.

C. Drop lifetimes

The exploration of drop dynamics presented in Sec. IV A was done for many points of the (ν, Γ) phase diagram, as shown in Fig. 8. During this exploration, once the drop was positioned on top of the NPHS and it was observed to be stable, the recordings were limited to 2 s at 400 fps. The three cases that were observed—regular periodic bouncing, period doubling, and chaotic/erratic dynamics—should then be considered as stable cases over lifetimes of at least a few seconds, as some time is required after the drop positioning and the camera recording initiation. During these experiments, we also observed that when the drop was not removed manually, in most cases it can

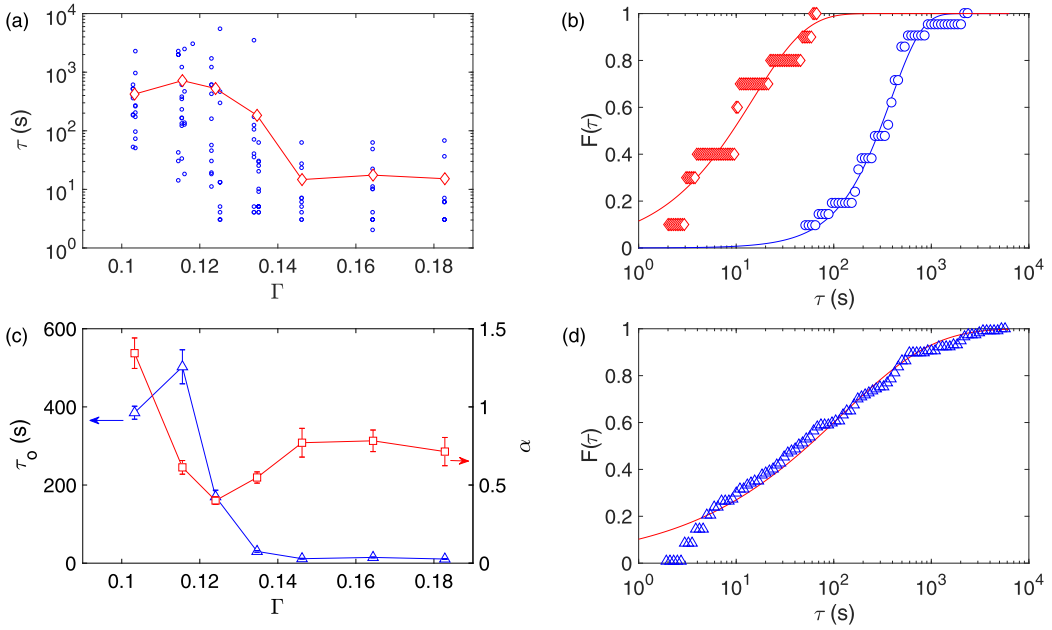

FIG. 15. (a) Measured lifetimes τ as a function Γ. Symbols represent the individual τ measurements ($\circ$) and their averages $\langle\tau\rangle$ ($\diamond$) for different accelerations. (b) Cumulative distribution function for $\Gamma = 0.103$ ($\circ$) and $\Gamma = 0.164$ ($\diamond$). The solid lines are fits to the Weibull function $F(\tau) = 1 - e^{-(\tau/\tau_o)^{\alpha}}$, with $\tau_o = 385.1 \pm 16.7$ s, $\alpha = 1.34 \pm 0.10$, and $R^2 = 0.985$ for $\Gamma = 0.103$, and $\tau_o = 14.7 \pm 1.1$ s, $\alpha = 0.78 \pm 0.07$, and $R^2 = 0.923$ for $\Gamma = 0.164$, where R^2 is the regression coefficient. (c) Double plot of the scale and shape factors, τ_o ($\triangle$) and α ($\square$), as a function of Γ. (d) Lifetime cumulative distribution function for all of the 117 realizations. The solid line is the fit to the Weibull function, with $\tau_o = 120.7 \pm 9.6$ s, $\alpha = 0.47 \pm 0.02$, and $R^2 = 0.980$.

bounce for some minutes and, on some occasions, with lifetimes as long as 90 min, implying that the juggling soliton has lifetimes between 10^2 and 2.7×10^4 rebounds.

In order to further characterize the drop dynamics and the possible dynamical states, we did a series of longer measurements, at fixed frequency, with drops of diameter $D \approx 2.5$ mm and for several accelerations in the range $\Gamma = 0.103$–0.183. In total, 117 stable bouncing drop realizations where recorded and analyzed. We selected the forcing frequency $f = 10.3$ Hz because it has the richest dynamical behavior over a larger acceleration range during the previous phase-space exploration. The procedure is similar to before, but now we left the drops to bounce until their death, i.e., until they coalesce with the liquid bath. Images were recorded for 10 s at 500 fps every few minutes. The longest realization of all these 117 stable juggling solitons had a lifetime of about 5410 s $\approx$ 90 min, consistent with previous observations.

In Fig. 15, we present the summary of the lifetime survey. Measurements of lifetimes τ and their averages $\langle\tau\rangle$ as functions of Γ are presented in Fig. 15(a). There is a large variability in measurements, with τ varying by about two orders of magnitude for each acceleration. In the lower-Γ range, from 0.1 to $\approx$0.13, the juggling solitons are more stable with longer lifetimes, which could be a consequence of the dominance of the regular periodic bouncing state [see Fig. 11(b)]. Terwagne *et al.* [5] did experiments below the Faraday threshold with a more viscous liquid, with kinematic viscosity 50 times the one of water, and also showed that longer lifetimes occur at lower accelerations. Additionally, they observed that lifetimes also decrease when the driving frequency increases. By analyzing the air-film thickness, the drop center-of-mass motion, and its deformation during the drop liquid-bath contact time, they demonstrated that short lifetimes are correlated to a small air-film thickness and to a large phase offset between the maximum of drop deformation and

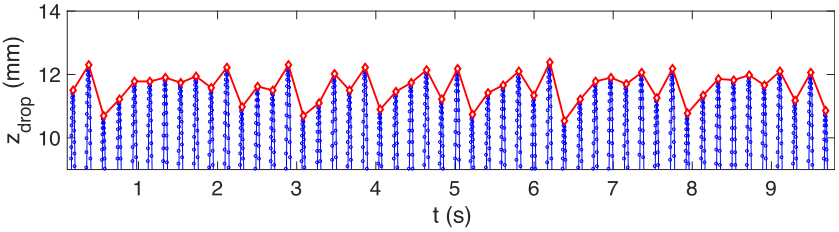

FIG. 16. Example of a sawtooth state, $f = 10.3$ Hz and $\Gamma = 0.118$. Small symbols ($\circ$) joined by thin lines correspond to the drop's center-of-mass vertical position vs time. Just the values around the local maxima are shown. Each parabola corresponds to a drop free flight above the NPHS. Larger symbols ($\diamond$) joined by thick lines are the local maxima. About 50 rebounds are observed in a 10 s time lapse.

the minimum of the vertical position of its center of mass. For fixed forcing parameters, they also demonstrated that the lifetimes follow a Weibull distribution, which obeys the following cumulative distribution function:

$$F(\tau) = 1 - e^{-(\tau/\tau_o)^\alpha}, \tag{4}$$

where τ_o and α are the scale and shape factors, respectively. The cumulative Poisson distribution is obtained for $\alpha = 1$.

Our data are also consistent with the Weibull distribution, as shown in Fig. 15(b) for $\Gamma = 0.103$ and $\Gamma = 0.164$. The data binning is done over 100 segments equally spaced in a logarithmic scale, from the minimum to the maximum τ. Figure 15(c) presents the fitted parameters τ_o and α as functions of Γ. For all Γ, we obtain $\alpha < 1$, except at $\Gamma = 0.103$, for which $\alpha = 1.34 \pm 0.10$. A shape factor $\alpha < 1$ implies a death process that is very sensitive to initial conditions, whereas $\alpha > 1$ means that the death process is by aging [5]. It seems interesting that at least for the lowest acceleration presented in this study, at its most stable, the drop's death process could be determined by air-film thickness aging of some sort, which remains to be studied in more detail. The fact that for higher Γ the death process depends on the initial conditions is confirmed by our experience at creating either stable or not so stable bouncing drops; the outcome does strongly depend on the correct timing between the drop release, its height, and the NPHS sloshing motion. On the other hand, the maximum average lifetime $\langle\tau\rangle$ occurs at $\Gamma = 0.116$, consistent with the maximum of τ_o at this acceleration, which quickly decreases from about 500 s to 10–30 s in a relatively small acceleration range, namely, after a 16% increase of Γ from 0.116 to 0.135. Finally, in Fig. 15(d), we present the cumulative distribution function for all of the 117 lifetime measurements (thus, for all Γ). It also obeys the Weibull distribution, as shown by the fitted curve, over three orders of magnitude in time. There is a clear mismatch at low lifetimes that could be due to a selection bias, since we only recorded once the drop already survived for some seconds.

D. Sawtooth and period tripling states

We now turn to the characterization of some new states that we observed during the long-time measurements campaign. First, we introduce a new longtime living state that we have named sawtooth state, an example of which is presented in Fig. 16. Besides its long time stability, its main dynamical feature is its sustained maximum soliton height growth, for a few cycles, followed by a more abrupt decrease in this maximum height; the drop's maximum height follows a sawtooth shape, with some added noise. This is emphasized in Fig. 16 by the red diamonds joined by red solid lines in the drop's maximum height. This sawtooth state can be quite stable, with a lifetime of about 3000 s in this case.

In Fig. 17(a), we present the maximum height variations as a function of the phase difference with respect to the one of the maximum height for each video of the sawtooth state. The procedure is the

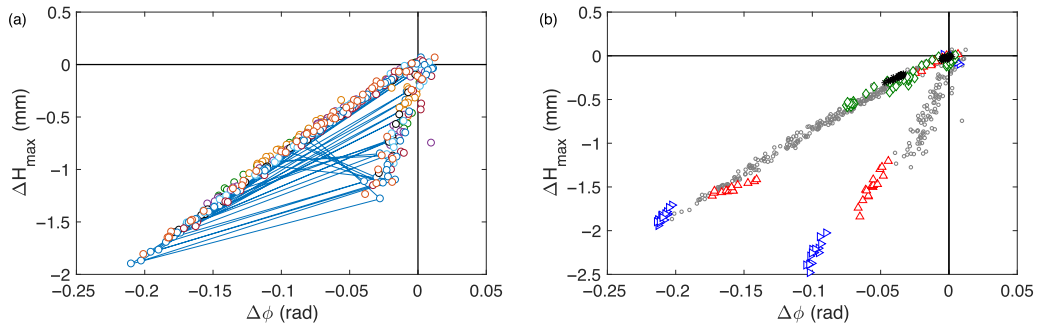

FIG. 17. (a) Plot of height variations $\Delta H_{\max}$, with respect to the sawtooth maximum value, vs the phase difference $\Delta\phi$, for each video acquisition obtained every few minutes during the whole juggling soliton lifetime. Each symbol color represents a different video acquisition. The solid line shows the jumps from one branch to another for one of the video acquisitions. (b) Same as in (a), but additional to the sawtooth state ($\circ$), we present two period doubling realizations ($*$, $\diamond$) and two tripling period states ($\triangle$). All these short living states collapse on either of the two branches of the sawtooth state or on extensions of them.

following: the three largest heights in a sawtooth state time series, as the one shown in Fig. 16, are averaged. Then, to each maximum drop height H_n, we subtract this average, obtaining $\Delta H_{\max}$, which by definition is, in general, negative. The π-unwrapped phase for each of these three maxima is also averaged. Then, to the π-unwrapped phase of each H_n, we subtract this average phase, obtaining $\Delta\phi$. This locates the maxima of each sawtooth state time series around (0,0) in this phase representation. For example, a regular periodic state shows up as a cloud of points closely around (0,0), with a predominance of negative values due to their definitions. The sawtooth state clearly shows a defined structure with this representation, with two branches that meet at (0,0). The sawtooth state drop heights are observed to jump alternating from one branch to another as the dynamic evolves, as shown for one of the time series (thus, for one of the videos taken every few minutes), with solid lines between the symbols.

During this long-time measurement campaign, we also observed period doubling and period tripling states, with typical lifetimes in the range of 10–300 s. Interestingly, when these states are plotted in the $\Delta H_{\max}$ versus $\Delta\phi$ representation, the data seem to collapse on the two branches of the sawtooth state or even on extensions of them. This is shown in Fig. 17(b). Here, the small circles $\circ$ (in gray) correspond to the previous sawtooth state. Additionally, two period doubling states are shown. The asterisks correspond to one that was stable over the 10-s measurement done shortly after the juggling soliton was created. The data split in two regions, one around (0,0) and the other at a certain distance on the top branch. The other period doubling state, shown with symbols $\diamond$, corresponds to a realization of a transition from a regular periodic state to a period doubling one. The initial state is located around $(-0.03, -0.3)$, and then the data separate into a group around the origin and another further away in the same branch, alternating every period between these two regions. Two period tripling states are also shown, with symbols $\triangle$. These define each of the three regions, with one around (0,0) and the other two at the end of each branch. An explanation for the collapse of this data in this representation requires further research.

V. CONCLUSIONS

We have proven that a nonpropagating hydrodynamic soliton can interact with droplets artificially placed on top of them. The soliton relaunches a drop into the air in every cycle of its motion in a juggling fashion and for long periods of time, with no coalescence of the drop with the liquid bath. We have provided a state phase space for the juggling soliton that includes three different dynamical regimes for the drop's trajectory: periodic, periodic doubling, and erratic. We have

studied and characterized these dynamics using histograms and return maps, and have presented the occupation fraction for the points of highest interest of these three dynamics. To understand the stability of this new structure, we have demonstrated that there is a synchronization and detuning of the drop's oscillation frequency with the soliton frequency. We speculate that this synchronization and detuning ensures stability and longer lifetimes. Then, we have analyzed the lifetime of the drop, concluding that the periodic behavior, which appears for the lowest-amplitude solitons, is the most stable bouncing state. Further analysis shows that lifetimes follow a Weibull distribution. Finally, during the long-time measurements, we discovered two new dynamic states, the sawtooth and the period tripling states. These show exciting and richer features, require new ways of characterization, and make even more interesting the juggling soliton's phase space.

The juggling soliton has another outstanding feature: it confines the motion of the bouncing drops. Drops gently blown away from their equilibrium position at the wave maximum are quickly pulled back to their original location. The dynamic bond state between the drop and the localized wave is reminiscent of optical tweezers. Indeed, the significant perturbation that the drop produces on the surface wave after every impact recalls how scattered waves affect the radiation pressure around confined particles by light beams. The juggling soliton can also trap two drops with their equilibrium position symmetrically shifted away from the soliton center, with drops visibly interacting via a long-range field sustained on the surface wave. The described behaviors are systematically observed; hence, there is compelling evidence that the juggling soliton is a one-dimensional (1D) hydrodynamic analog of optical tweezers. Further experimental characterization of lateral droplet dynamics and a theoretical understanding of drop bouncing on large amplitude wave fields are the next key steps to determining the strength of the field that confines bouncing drops.

ACKNOWLEDGMENTS

The authors are thankful for the financial support of FONDECYT Grant No. 1180636. We also acknowledge Fondecyt Grant No. 1160823 for the use of the Shape Drop Analyzer.

[1] J. Walker, Drops of liquid can be made to float on the liquid. What enables them to do so? Sci. Am. **238**(6), 151 (1978).
[2] M. Faraday, XVII. On a peculiar class of acoustical figures; and on certain forms assumed by groups of particles upon vibrating elastic surfaces, Phil. Trans. R. Soc. Lond. **121**, 299 (1831).
[3] S. Douady, Experimental study of the Faraday instability, J. Fluid Mech. **221**, 383 (1990).
[4] Y. Couder, E. Fort, C.-H. Gautier, and A. Boudaoud, From Bouncing To Floating: Noncoalescence of Drops On A Fluid Bath, Phys. Rev. Lett. **94**, 177801 (2005).
[5] D. Terwagne, N. Vandewalle, and S. Dorbolo, Lifetime of a bouncing droplet, Phys. Rev. E **76**, 056311 (2007).
[6] J. Moláček and J. W. M. Bush, Drops bouncing on a vibrating bath, J. Fluid Mech. **727**, 582 (2013).
[7] D. Terwagne, F. Ludewig, N. Vandewalle, and S. Dorbolo, The role of the droplet deformations in the bouncing droplet dynamics, Phys. Fluids **25**, 122101 (2013).
[8] M. Hubert, D. Robert, H. Caps, S. Dorbolo, and N. Vandewalle, Resonant and antiresonant bouncing droplets, Phys. Rev. E **91**, 023017 (2015).
[9] Y. Couder, S. Protiere, E. Fort, and A. Boudaoud, Dynamical phenomena: Walking and orbiting droplets, Nature (London) **437**, 208 (2005).
[10] S. Protière, A. Boudaoud, and Y. Couder, Particle-wave association on a fluid interface, J. Fluid Mech. **554**, 85 (2006).
[11] Y. Couder and E. Fort, Single-Particle Diffraction And Interference At A Macroscopic Scale, Phys. Rev. Lett. **97**, 154101 (2006).

[12] A. Andersen, J. Madsen, C. Reichelt, S. Rosenlund Ahl, B. Lautrup, C. Ellegaard, M. T. Levinsen, and T. Bohr, Double-slit experiment with single wave-driven particles and its relation to quantum mechanics, Phys. Rev. E **92**, 013006 (2015).
[13] A. Eddi, E. Fort, F. Moisy, and Y. Couder, Unpredictable Tunneling of A Classical Wave-Particle Association, Phys. Rev. Lett. **102**, 240401 (2009).
[14] A. Eddi, J. Moukhtar, S. Perrard, E. Fort, and Y. Couder, Level Splitting At Macroscopic Scale, Phys. Rev. Lett. **108**, 264503 (2012).
[15] D. M. Harris, J. Moukhtar, E. Fort, Y. Couder, and J. W. M. Bush, Wavelike statistics from pilot-wave dynamics in a circular corral, Phys. Rev. E **88**, 011001(R) (2013).
[16] D. M. Harris and J. W. M. Bush, Droplets walking in a rotating frame: From quantized orbits to multimodal statistics, J. Fluid Mech. **739**, 444 (2014).
[17] P. J. Sáenz, T. Cristea-Platon, and J. W. M. Bush, Statistical projection effects in a hydrodynamic pilot-wave system, Nat. Phys. **14**, 315 (2018).
[18] P. J. Sáenz, G. Pucci, S. E. Turton, A. Goujon, R. R. Rosales, J. Dunkel, and J. W. M. Bush, Emergent order in hydrodynamic spin lattices, Nature (London) **596**, 58 (2021).
[19] E. Fort, A. Eddi, A. Boudaoud, J. Moukhtar, and Y. Couder, Path-memory induced quantization of classical orbits, Proc. Natl. Acad. Sci. **107**, 17515 (2010).
[20] A. Eddi, E. Sultan, J. Moukhtar, E. Fort, M. Rossi, and Y. Couder, Information stored in Faraday waves: The origin of a path memory, J. Fluid Mech. **674**, 433 (2011).
[21] D. M. Harris and J. W. M. Bush, The pilot-wave dynamics of walking droplets, Phys. Fluids **25**, 091112 (2013).
[22] A. U. Oza, R. R. Rosales, and J. W. M. Bush, A trajectory equation for walking droplets: Hydrodynamic pilot-wave theory, J. Fluid Mech. **737**, 552 (2013).
[23] M. Labousse, A. U. Oza, S. Perrard, and J. W. M. Bush, Pilot-wave dynamics in a harmonic potential: Quantization and stability of circular orbits, Phys. Rev. E **93**, 033122 (2016).
[24] J. W. Bush, Pilot-wave hydrodynamics, Annu. Rev. Fluid Mech. **47**, 269 (2015).
[25] J. W. M. Bush and A. U. Oza, Hydrodynamic quantum analogs, Rep. Prog. Phys. **84**, 017001 (2020).
[26] N. Sungar, L. D. Tambasco, G. Pucci, P. J. Sáenz, and J. W. M. Bush, Hydrodynamic analog of particle trapping with the Talbot effect, Phys. Rev. Fluids **2**, 103602 (2017).
[27] L. D. Tambasco, J. J. Pilgram, and J. W. M. Bush, Bouncing droplet dynamics above the Faraday threshold, Chaos: Interdiscipl. J. Nonlin. Sci. **28**, 096107 (2018).
[28] X. Zhao, J. Tang, and J. Liu, Electrically switchable surface waves and bouncing droplets excited on a liquid metal bath, Phys. Rev. Fluids **3**, 124804 (2018).
[29] J. Wu, R. Keolian, and I. Rudnick, Observation of A Nonpropagating Hydrodynamic Soliton, Phys. Rev. Lett. **52**, 1421 (1984).
[30] W. Wang, X. Wang, J. Wang, and R. Wei, Dynamical behavior of parametrically excited solitary waves in Faraday's water trough experiment, Phys. Lett. A **219**, 74 (1996).
[31] M. G. Clerc, S. Coulibaly, N. Mujica, R. Navarro, and T. Sauma, Soliton pair interaction law in parametrically driven Newtonian fluid, Phil. Trans. R. Soc. A. **367**, 3213 (2009).
[32] M. G. Clerc, S. Coulibaly, L. Gordillo, N. Mujica, and R. Navarro, Coalescence cascade of dissipative solitons in parametrically driven systems, Phys. Rev. E **84**, 036205 (2011).
[33] H. Arbell and J. Fineberg, Temporally Harmonic Oscillons In Newtonian Fluids, Phys. Rev. Lett. **85**, 756 (2000).
[34] J. Rajchenbach, A. Leroux, and D. Clamond, New Standing Solitary Waves In Water, Phys. Rev. Lett. **107**, 024502 (2011).
[35] J. W. Miles, Parametrically excited solitary waves, J. Fluid Mech. **148**, 451 (1984).
[36] I. V. Barashenkov, M. M. Bogdan, and V. I. Korobov, Stability diagram of the phase-locked solitons in the parametrically driven, damped nonlinear Schrödinger equation, Europhys. Lett. **15**, 113 (1991).
[37] B. Denardo, B. Galvin, A. Greenfield, A. Larraza, S. Putterman, and W. Wright, Observations of Localized Structures In Nonlinear Lattices: Domain Walls And Kinks, Phys. Rev. Lett. **68**, 1730 (1992).

[38] L. Gordillo, T. Sauma, Y. Zárate, I. Espinoza, M. Clerc, and N. Mujica, Can nonpropagating hydrodynamic solitons be forced to move? Europhys. J. D **62**, 39 (2011).
[39] L. Zhang, X. Wang, and Z. Tao, Spatiotemporal bifurcations of a parametrically excited solitary wave, Phys. Rev. E **75**, 036602 (2007).
[40] W. Chen, J. Tu, and R. Wei, Onset instability to nonpropagating hydrodynamic solitons, Phys. Lett. A **255**, 272 (1999).
[41] L. Gordillo and N. Mujica, Measurement of the velocity field in parametrically excited solitary waves, J. Fluid Mech. **754**, 590 (2014).
[42] L. Gordillo, Nonpropagating hydrodynamic solitons in a quasi-one-dimensional free surface subject to vertical vibrations, Ph.D. thesis, Universidad de Chile, 2012.
[43] M. G. Cabezas, A. Bateni, J. M. Montanero, and A. W. Neumann, A new method of image processing in the analysis of axisymmetric drop shapes, Colloids Surf., A **255**, 193 (2005).
[44] See Supplemental Material at http://link.aps.org/supplemental/10.1103/PhysRevFluids.8.024401 for videos of the experiment.
[45] E. Becker, W. J. Hiller, and T. A. Kowalewski, Experimental and theoretical investigation of large-amplitude oscillations of liquid droplets, J. Fluid Mech. **231**, 189 (1991).